metals

MDPI

Article

Fluid Dynamics Analysis of Coherent Jet with a Mixed Shrouding H_2-CO_2/N_2 for EAF Steelmaking

Songtao Yan [1,2], Fuhai Liu [1,2,3,*], Rong Zhu [2,3], Guangsheng Wei [2,3,*] and Kai Dong [2,3]

[1] National Center for Materials Service Safety, University of Science and Technology Beijing, Beijing 100083, China
[2] Institute for Carbon Neutrality, University of Science and Technology Beijing, Beijing 100083, China
[3] Institute of Steel Sustainable Technology, Liaoning Academy of Materials, Shenyang 110167, China
* Correspondence: liufuhaisteel@ustb.edu.cn (F.L.); wgsustb2007@163.com (G.W.)

Abstract: In order to suppress the rapid combustion effect and consumption rate of pure hydrogen gas, N_2 or CO_2 at flow rates of 0, 80, and 240 Nm^3/h was pre-mixed with shrouding H_2 at flow rates of 800, 720, and 560 Nm^3/h at room temperature, and the behaviors of the main oxygen jet and shrouding flame were analyzed by both numerical simulation and combustion experiments. The results showed that, because of the participation of CO_2 in the H_2 combustion reaction, the length of the axial velocity potential core was reduced using the CO_2 shrouding mixed injection method, compared to the same mixed rate of N_2. This trend would be further enhanced as N_2 and CO_2 mixing ratio increased. Meanwhile, when the shrouding mixed rate is 30%, the maximum axial and radial expansion rate generated by N_2-H_2 shrouding method is 1.28 and 1.04 times longer than that by the CO_2-H_2 shrouding method. The $F_{o\text{-}a}$, theoretical impaction depth and area generated by the 10% N_2 shrouding mixed rate was 84.0, 95.5 and 86.4% of those generated by the traditional coherent jet, respectively, which indicated that the 10% N_2 shrouding mixed rate method might lead to comparable production indexes in the EAF steelmaking process.

Keywords: EAF; coherent lance; H_2; mixing

check for updates

Academic Editor: Yasar Kocaefe

Received: 8 February 2025
Revised: 5 March 2025
Accepted: 6 March 2025
Published: 7 March 2025

Citation: Yan, S.; Liu, F.; Zhu, R.; Wei, G.; Dong, K. Fluid Dynamics Analysis of Coherent Jet with a Mixed Shrouding H_2-CO_2/N_2 for EAF Steelmaking. *Metals* **2025**, *15*, 291. https://doi.org/10.3390/met15030291

Copyright: © 2025 by the authors. Licensee MDPI, Basel, Switzerland. This article is an open access article distributed under the terms and conditions of the Creative Commons Attribution (CC BY) license (https://creativecommons.org/licenses/by/4.0/).

1. Introduction

In comparison to the structure of the Basic Oxygen Furnace (BOF), a flat structure is applied in the Electrical Arc Furnace (EAF), which is designed to ease the process of changing scrap steel, providing a three-phase electrode supply, and enabling the tapping of molten steel [1–4]. This indicates that the top-blowing oxygen supplement for the BOF steelmaking process is not directly used in the EAF steelmaking process. Therefore, the EAF steelmaking process has adopted the side-blowing method with multiple oxygen lances to enhance the dynamic conditions and mass transfer rate in the molten bath. In order to further improve the impaction ability and utilization rate of the oxygen supersonic jet, a shrouding combustion technology utilizing gas or liquid fuel has been developed and extensively applied in the EAF steelmaking process, known as coherent lance technology [5–7].

Many previous studies have focused on optimizing geometric structure and operational methods for coherent lance technology. Yamaguchi et al. [8] highlighted the advantages of using a coherent lance structure for heating low-temperature steel scrap and providing kinetic energy, in contrast to the traditional supersonic lance structure. Tian et al. [9] investigated the influence of various lime powder injection rates and central nozzle diameters on the flow field of the coherent jet. Wei et al. [10] proposed a mathematical model to describe the relationship between the operational conditions, such as lance height,

design velocity, and the exit diameter of the Laval nozzle, and the impaction depth of the molten bath generated by the coherent jet. Jung et al. [11] presented a new jet-burner technology for coherent lance, which effectively reduced splashing and disturbance of electric arcs during melting, as demonstrated in a small-sized EAF.

The only byproduct of hydrogen combustion is water, rendering it a zero-emission energy source. Concurrently, hydrogen energy has the potential to diversify the energy portfolio and reduce reliance on fossil fuels. These characteristics position hydrogen energy as a pivotal solution for decreasing greenhouse gas emissions and improving air quality [12–15]. This implies that the shrouding fuel gas can be composed entirely of green H_2, allowing for a 100% volume fraction. Feng et al. [16] introduced the different behavior of the coherent jet generated by H_2 and CH_4 shrouding gas and pointed out that the heat utilization of H_2 shrouding gas was suppressed due to its higher combustion rate. Mahoney et al. [17] highlighted the critical role of H_2 in coherent lance technology and demonstrated that employing H_2 in the coherent lance could accelerate the decarburization rate and enhance the effectiveness of slag-metal stirring in the EAF steelmaking process.

Although a coherent lance using H_2 is beneficial for enhancement of the technical and economical index in the EAF steelmaking process, low-cost and large-scale production of green H_2 is still a great challenge. Previous studies have indicated that employing the N_2-CH_4 mixed shrouding injection method can lead to comparable production indexes in the EAF steelmaking process, as demonstrated through a series of industrial application tests [18].

To enhance the utilization rate of H_2 and reduce its consumption, the effect of the mixed shrouding injection method on the flow field of the coherent jet has been investigated in this paper. Based on the physicochemical properties of N_2 and CO_2, N_2 is considered an inert gas, signifying that no intermediate products are formed by the reaction of N_2 with H_2. In contrast, CO_2 actively participates in the combustion reaction of H_2, leading to the formation of unstable compounds, like OH, CO and HCO, in a very brief timespan [19–21]. Therefore, both the N_2-H_2 and CO_2-H_2 mixed shrouding injection methods have been analyzed by numerical simulation and combustion experiments in this research, to determine a suitable mixed shrouding injection method for the coherent lance method.

In this paper, Section 2 presents the coherent lance structure, illustrating the arrangement of the shrouding nozzles and providing a brief introduction to the combustion experiment. Section 3 outlines the detailed conditions of the numerical model. Subsequently, the axial velocity, total temperature, theoretical impaction cavity shape and the effective oxygen flow rate achieved by the simulation model are intensively investigated in Sections 4.1–4.3. Finally, Section 5 concludes the research by presenting the main findings.

2. Coherent Lance and Experimental System

According to the operational conditions of the 120 t EAF, the design Mach number and the main oxygen flow rate of the coherent lance (Keda Machinery Manufacturing Co., Ltd., Bazhou, Hebei, China) were determined to be 2.20 and 2500 Nm^3/h, respectively. The throat and exit radiuses of the main Laval nozzle, calculated by one-dimensional iso-entropic flow theory, were 11.1 and 15.7 mm, respectively.

In this research, the shrouding nozzle structure was designed as a three concentric rings arrangement, their radiuses from the inner to the outer concentric ring being 34.0, 49.5, and 64.0 mm, respectively, as shown in Figure 1. Moreover, the hydraulic radiuses of the inner, intermediate and outer shrouding nozzles were 4.4, 5.6 and 6.8 mm, respectively, and there were 10 shrouding nozzles at each concentric ring.

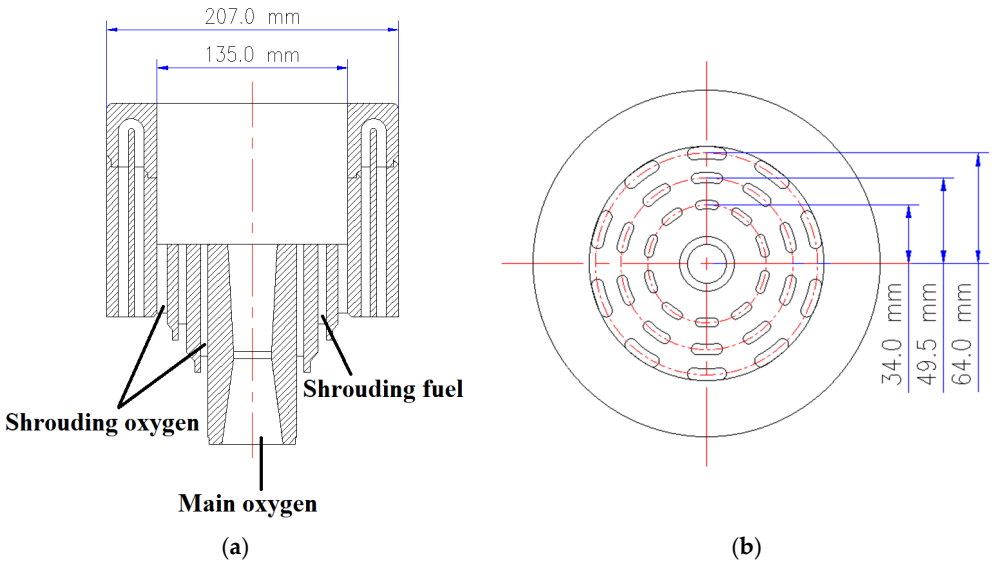


Figure 1. Cross view (**a**) and front view (**b**) of the coherent lance.

Table 1 presents the details of the operational conditions of the combustion experiment. Three mixed types have been selected, which were 0, 10 and 30% volume fractions of the design H_2 shrouding flow rate. Thus, the CO_2 and N_2 mixed flow rates were set at 0, 80 and 240 Nm^3/h, respectively, while the H_2 shrouding flow rates were 800, 720 and 560 Nm^3/h, respectively. Additionally, the O_2 shrouding flow rate was set at half that of the H_2 shrouding flow rate.

Table 1. Operational conditions.

Label	Type of Detail Conditions	Values
Main Laval nozzle	Flow rate (Nm^3/h)	2500
	Mach number	2.20
	Oxygen temperature (K)	300
Fuel shrouding nozzle	H_2 flow rate (Nm^3/h)	800/720/560
	N_2 flow rate (Nm^3/h)	0/80/240
	CO_2 flow rate (Nm^3/h)	0/80/240
	Gas flow temperature (K)	300
Oxygen shrouding nozzle	Flow rate (Nm^3/h)	400/360/280
	Gas flow temperature (K)	300

Both inner and outer shrouding nozzles are used to transport oxygen, and the shrouding fuel gas was injected by the intermediate shrouding nozzle. The same parameters for the coherent lance were used in both the numerical simulations and combustion experiments. This indicated that both numerical simulation and combustion experiments were carried out with a full-scale coherent lance.

In this research, a series of combustion experiments was conducted in a high-temperature combustion furnace (Keda Machinery Manufacturing Co., Ltd., Bazhou, Hebei, China), as depicted in Figure 2. In the preparation stage, the burner was ignited to improve the ambient temperature of experimental furnace, and 12 thermocouples were fixed at different locations of the furnace side-wall, as shown in Figure 2a,b.

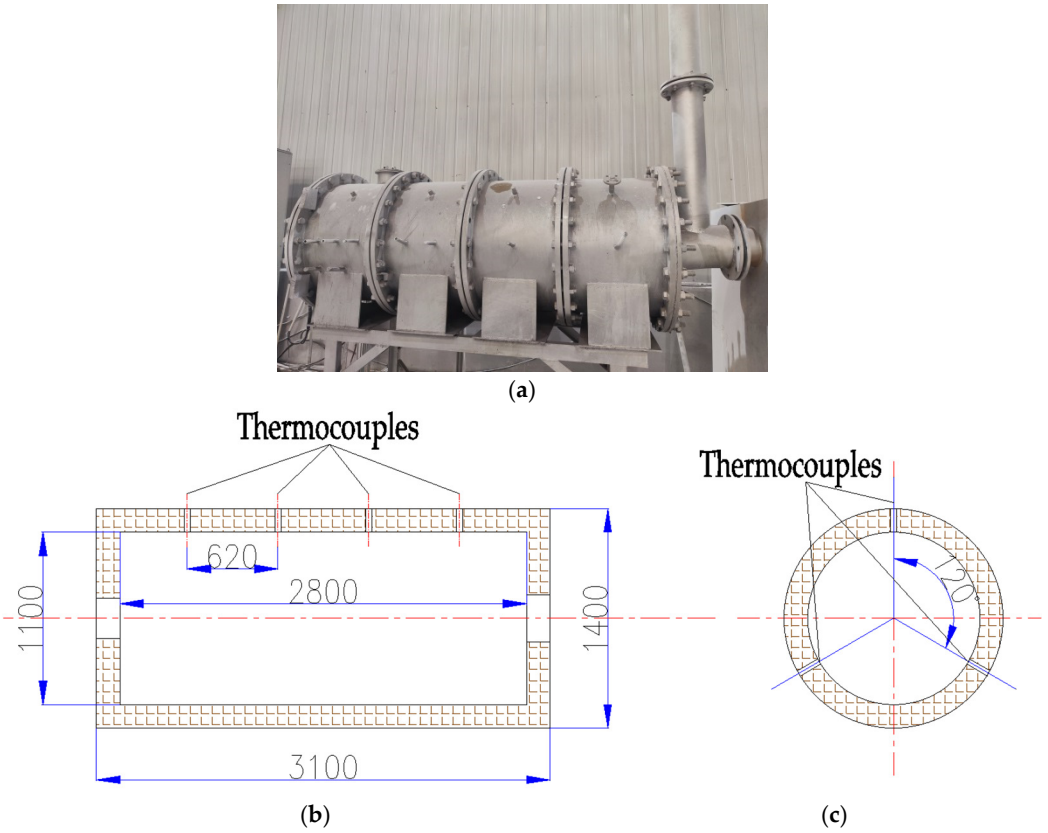


Figure 2. The (**a**) physical diagram, (**b**) front view and (**c**) cross view of the high temperature combustion furnace. (Unit: mm).

When the ambient temperature reached 1700 K, the burner was extinguished. The Pitot tube was initially positioned at specific axial locations to measure the dynamic and static pressures of the coherent jet along the centerline of the Laval nozzle. Subsequently, a thermocouple was placed at the same locations in order to measure the total temperature of the coherent jet. Finally, a hollow tube replaced the thermocouple to measure the gas content. Based on the pressure, temperature and gas content, the axial velocity of the coherent jet was calculated by Equations (1)–(3), following [22].

$$V = \sqrt{\frac{2\gamma RT}{\gamma - 1}\left[\left(\frac{P_d}{P_s}\right)^{(\gamma-1)/\gamma} - 1\right]}, \text{ Ma } > 0.3, \tag{1}$$

$$V = \sqrt{\frac{2(P_t - P_s)}{\rho}}, \text{ Ma } \leq 0.3, \tag{2}$$

$$\gamma = \sum_{i=1}^{n} (\gamma_i \times m_{f-i}) \tag{3}$$

The pressure, temperature, and oxygen mass fraction of the coherent jet were measured continuously for 10 s. Combustion experiments under each operational condition were conducted three times. After calculating the average values of these measurements, they were compared with the simulation results to evaluate the accuracy of the numerical model. In previous literature [10,16,18], the measurement method and experimental system details have been reported and are only briefly mentioned here.

3. Numerical Model

To leverage the symmetry of the simulation model and reduce computational costs, only one-quarter of the geometry was used. A three-dimensional (3D) grid comprising 3.38 million hexahedral cells was then constructed. A Laval nozzle, comprising contraction, throat, and expansion sections, was constructed. Additionally, shrouding nozzles with a length of 100 mm were also incorporated into the simulation model. The high-velocity jet region extends from the tip of the main Laval nozzle to a distance of 2100 mm downstream in the axial direction and 400 mm in the radial direction, as illustrated in Figure 3a.

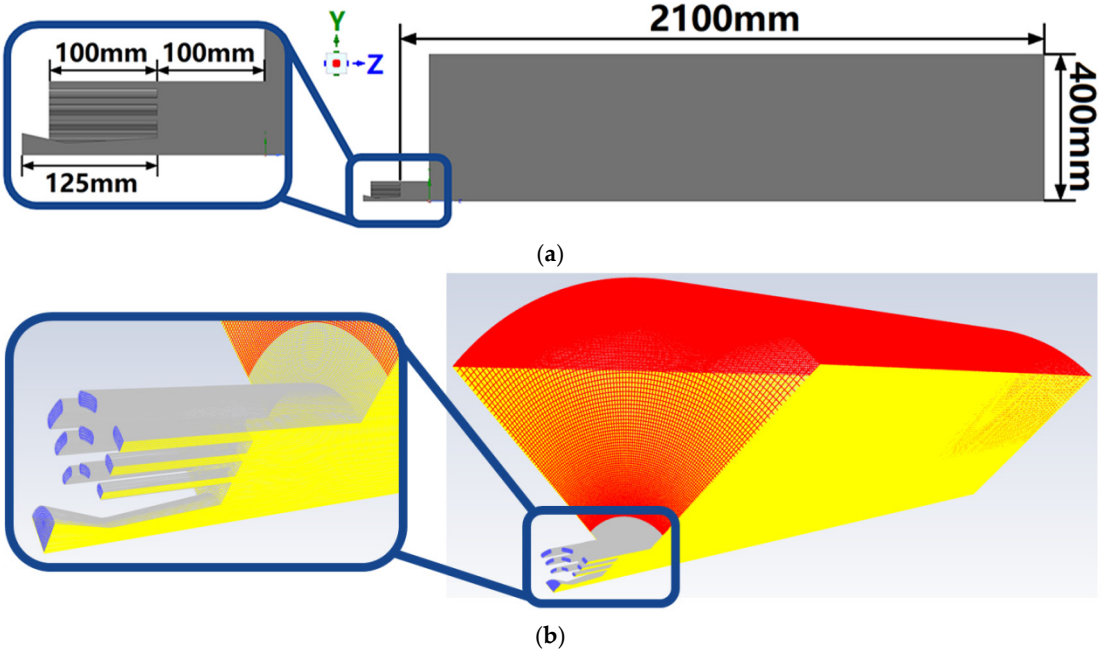


Figure 3. (**a**) Geometric construction of the numerical model. (**b**) Mesh profile of the numerical model with boundary conditions.

Figure 3b depicts the grid distribution of the numerical model with boundary conditions. The mass flow inlet was used at the main Laval and shrouding nozzle inlet (blue plane). The pressure outlet was adopted for the other computational domain boundaries (red plane). A non-slip condition was implemented at the coherent lance wall (gray plane) for the wall boundary condition.

Hereafter, the operational condition of the coherent lance was addressed by the shrouding gas flow rate and type. For instance, "H720-N80" represented that the flow rates of the H_2 and N_2 shrouding gas were 720 and 80 Nm^3/h, respectively. Moreover, "H560-C240" represented that the flow rates of the H_2 and CO_2 shrouding gas were 560 and 240 Nm^3/h, respectively. The traditional supersonic jet generated by the coherent lance without any shrouding gas was abbreviated as "TRA". In all simulation scenarios, the oxygen flow rate through the main Laval nozzle was consistently set at 2500 Nm^3/h.

In this paper, the all-zone initialization method was utilized. The x-velocity, y-velocity, and z-velocity were all set to 0 m/s This indicates that the computational domain began without any gas flow through the Laval or shrouding nozzle and was initially filled solely with static air.

The flow field of the coherent jet was simulated in this research using the commercial CFD software FLUENT 2020 R2 (ANSYS, Inc., Pittsburgh, PA, USA). In order to achieve an accurate simulation result, the SST k-ω turbulence model was used to compute the flow dynamics of the coherent jet, which combined the advantages of both the standard k-ε model and standard k-ω model.

The mass flow inlet and pressure outlet were designated as the boundary conditions for the inlet and outlet, respectively. To obtain more accurate results, specifications for intensity and hydraulic diameter were applied. Additionally, the initial turbulent intensity and backflow turbulent intensity values at the inlet and outlet boundary conditions were set at 3.0% and 5.5%, respectively.

The reactants produced by the fuel gas and oxygen underwent chemical reactions in a boundary zone and at a chemical scale, which was comparable to the turbulent mixing scale, based on the operating condition of the coherent lance. Thus, the EDC (Eddy-Dissipation Concept) model was selected for the interactions between turbulent flow and chemistry process, which was determined to be suitable for simulating shrouding combustion in previous studies. During the combustion process among H_2, O_2 and CO_2, a large amount of unstable intermediate products, such as CHO, CH and HO, would be formed. In order to accurately simulate this process, the detailed chemical kinetic mechanism (GRI-Mech 3.0) was adopted in this research.

The simulation cases were conducted in the steady-state solution mode using a coupled algorithm to solve the governing equations with a second-order discretization mechanism. In addition, the solution converged when the following criterion was satisfied: The average total temperature and velocity variations at the outlet of computational domain were kept within 2.0 K and 1.0 m/s, respectively. The simulations were all conducted using a workstation equipped with a 192-core CPU and 240 GB of memory.

4. Results and Discussion

4.1. Axial Velocity Distribution

Figure 4 presents the axial velocity profiles of the main oxygen jet using different fuel mixed injection methods at the centerline of the Laval nozzle. For further understanding of the effect of the fuel mixed injection method on the flow field of the main oxygen jet, both the coherent jet with an H_2 flow rate of 800 Nm^3/h and the traditional supersonic jet are included in Figure 4a,b. This means that both simulation result and experimental data for H800 are consistent in Figure 4a,b, which is also the case for TRA.

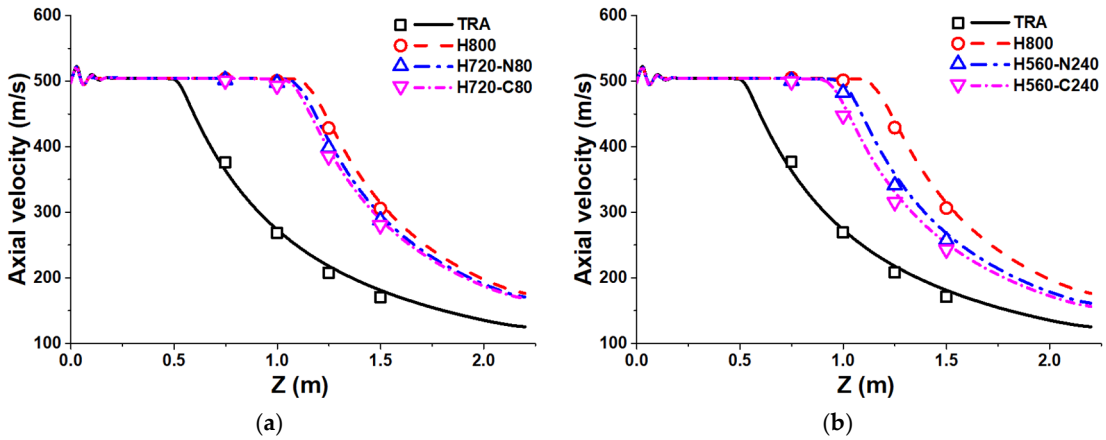


Figure 4. The axial velocity profiles of the main oxygen jet using different fuel mixed injection methods at the centerline of the Laval nozzle: (**a**) 10% shrouding fuel mixed method. (**b**) 30% shrouding fuel mixed method.

The various lines (solid and dotted lines) and symbols (□, ○, △ and ▽) represent the simulation and the result measurement data for the combustion experiment, respectively, in Figure 4.

It is crucial to recognize that maintaining a stable flow rate requires real-time adjustments to the valve system for gas supplementation. During this process, the measured

velocity value of the main oxygen jet exhibits continuous fluctuations within a defined range. The measurement data presented in Figure 4 represent only the average velocity calculated from the combustion experiment, as described in Section 2. Based on the experimental records, the observed deviation in the measured velocity value is ±6.2% of the average velocity.

Based on the result, the average axial velocity variation of the main oxygen jet at the centerline of the Laval nozzle between the experimental test and numerical simulation is about 4.3%, which proves that the experimental data is in good agreement with the simulation result. Thus, the numerical model built in this research can be adopted to accurately simulate the flow field of the coherent jet.

The results indicate that the shock wave first forms at the main Laval nozzle exit. Subsequently, the axial velocity potential core of the main oxygen jet is generated, due to its consistent axial velocity value. Finally, as the main oxygen jet reaches the end of the axial velocity potential core, its axial velocity continues to decrease. Based on the result, the initial axial velocities of the coherent jets at the Laval nozzle exit are the same at 499.5 m/s for all the operational conditions of the shrouding fuel mixed method. Hence, the shrouding fuel mixed method has no effect on the initial axial velocity of the main oxygen jet at the Laval nozzle exit.

The axial velocity potential core length of the main oxygen jet generated by H720-N80, H720-C80, H560-N240 and H560-C240 was 1.03, 1.01, 0.96 and 0.89 m, respectively. In addition, the axial velocity potential core length of the main oxygen jet generated by H800 and TRA was 1.09 and 0.49 m, respectively. Thus, the axial velocity potential core length of the main oxygen jet generated by H800 is 1.06, 1.08, 1.14 and 1.22 times longer than that generated by H720-N80, H720-C80, H560-N240 and H560-C240, respectively. Thus, the axial velocity potential core length of the main oxygen jet would be prolonged with a lower shrouding fuel mixed rate.

The result shows that the axial velocity potential core length of the main oxygen jet generated by H720-N80 and H560-N240 is 1.02 and 1.08 times longer, respectively, than that generated by H720-C80 and H560-C240. Thus, compared with the H_2-CO_2 shrouding mixed injection method, the axial velocity of the main oxygen jet generated by the H_2-N_2 shrouding mixed injection method is further reduced. Additionally, this trend becomes more pronounced with an increased shrouded mixed rate.

As an oxidizing gas, CO_2 will take part in the combustion reaction of the shrouding H_2. This process will lead to the formation of some unstable intermediate reaction products in a short timespan through the following reactions: $H + CO_2 \rightleftarrows O + HCO$, $OH + CO_2 \rightleftarrows HO_2 + CO$ and $H + CO_2 \rightleftarrows OH + CO$. It should be noted that these mentioned reactions are only part of the detailed reactions involving CO_2, O_2, and H_2.

Although these intermediate reaction products would be finally oxidized as H_2O and CO_2, parts of the thermal energy released by the surrounding H_2 combustion process are absorbed by these intermediate reaction products. As a result, the effectiveness of the shrouding combustion flame protection is decreased, thereby reducing the axial velocity potential core length and impaction ability of the main oxygen jet.

As mentioned, both the shrouding mixed rate and the type of shrouding mixed gas have a significant impact on the flow field of the coherent jet. The effect of the shrouding mixed injection method on the total temperature of the coherent jet will be further discussed in Section 4.2.

As the coherent jet passes through the ambient gas, its peripheral flow mixes with the ambient gas. During this process, the kinetic energy of the high-velocity coherent jet is absorbed by the low-velocity ambient gas. Thus, the axial velocity of the main oxygen jet at the centerline of the Laval nozzle cannot fully represent the decelerating characteristic of

the coherent jet velocity. In this paper, four crossing sections with Z coordinates of 1.00, 1.25, 1.50 and 1.75 m have been selected to calculate the average velocity of the coherent jet generated by various mixed injection methods, as depicted in Table 2.

Table 2. The average velocity of the coherent jet generated by various mixed injection methods.

Label	H800	TRA	H720-C80	H720-N80	H560-C240	H560-N240
1.00 m	216.8 m/s	134.1 m/s	204.4 m/s	208.7 m/s	184.8 m/s	194.6 m/s
1.25 m	173.0 m/s	110.3 m/s	163.2 m/s	166.4 m/s	148.1 m/s	155.2 m/s
1.50 m	140.1 m/s	93.5 m/s	132.7 m/s	135.0 m/s	121.7 m/s	126.7 m/s
1.75 m	114.9 m/s	80.6 m/s	109.6 m/s	111.2 m/s	101.8 m/s	105.2 m/s

Based on the simulation results calculated by the four crossing sections, the average velocity of the coherent jet generated by H800 is 1.04, 1.06, 1.11 and 1.16 times higher than that generated by H720-N80, H720-C80, H560-N240 and H560-C240, respectively. Thus, the average velocity of the coherent jet would be increased with a lower shrouding fuel mixed rate, as the mixing rate decreases from 30% to 0%.

Additionally, at the selected four crossing sections, the average velocity of the coherent jet generated by H720-N80 and H560-N240 is 1.02 and 1.05 times higher, respectively, than that generated by H720-C80 and H560-C240. This further proves that the impaction ability of coherent jet formed by the H_2-N_2 shrouding mixed injection method is better than that formed by the H_2-CO_2 shrouding mixed injection method.

4.2. Total Temperature Distribution

Figure 5 depicts the total temperature profiles of the main oxygen jet using different fuel mixed injection methods at the centerline of the Laval nozzle. Based on the experimental test (□, ○, △ and ▽) and numerical simulation (solid and dotted lines), the average total temperature variation of the main oxygen jet is 3.9%, which further proves good agreement between the experimental data and the simulation results.

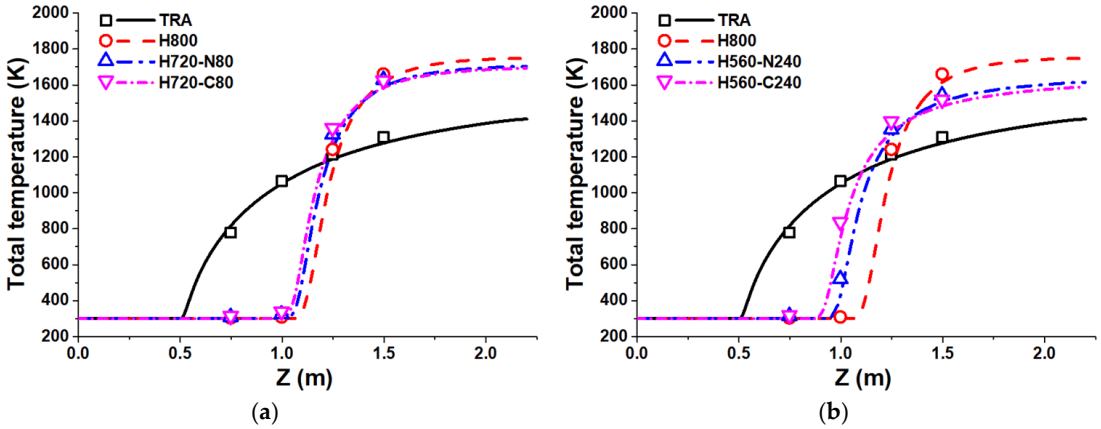


Figure 5. The total temperature of main oxygen profiles using different fuel mixed injection methods at centerline of the Laval nozzle: (**a**) 10% shrouding fuel mixed method. (**b**) 30% shrouding fuel mixed method.

After the main oxygen jet passes through the Laval nozzle, a potential core for total temperature is generated, similarly to the axial velocity potential core. Based on the result, the potential core lengths of the total temperature and axial velocity are same. This means that the main oxygen jet will quickly mix with the ambient gas when it reaches the end of the potential core, leading to an obvious acceleration in total temperature and deceleration in the axial velocity of the main oxygen jet.

With a longer potential core length, the peripheral main oxygen jet can absorb more thermal energy from the high-temperature combustion flame, within the potential core. As a result, the total temperature of the peripheral main oxygen jet is increased. After the main oxygen jet reaches the end of the potential core, the internal and peripheral main oxygen jets swiftly mix with each other. During this process, the total temperature acceleration rate of the internal main oxygen jet is further increased by a higher total temperature of the peripheral main oxygen jet. Thus, the total temperature of the main oxygen jet more quickly arrives at the ambient temperature of 1700 K when its potential core is longer, as illustrated in Figure 5.

Based on the calorific value of the shrouding fuel jet, the per second calorific values using H800, H720-N80, H720-C80, H560-N240 and H560-C240 was 8644, 7779, 7779, 6050 and 6050 MJ/s, respectively. Meanwhile, the simulation result shows that the maximum total temperature of the shrouding combustion flame was 2970, 2922, 2857, 2753 and 2536 K, respectively. Hence, the maximum total temperature of the shrouding combustion flame is reduced with a higher shrouding mixed rate.

When the shrouding mixed rate is 10% and 30%, the total temperature variation between the H_2-CO_2 and H_2-N_2 shrouding mixed injection method was 65 and 217 K, respectively. This indicates that the maximum total temperature of the shrouding combustion flame formed by the H_2-N_2 shrouding mixed injection method is higher than that by the H_2-CO_2 shrouding mixed injection method, at the same shrouding mixed rate.

As mentioned in Section 4.1, CO_2 is one kind of oxidizing gas, and will take part in the combustion reaction of the shrouding H_2 at a combustion temperature exceeding 1073 K, leading to the formation of unstable intermediate reaction products [23–25]. Thus, in order to research the effect of shrouding mixed rate and gas type on the flow field of the combustion flame, the total temperature of the coherent jet profiles using different fuel mixed injection methods is presented in Figure 6.

In this paper, both maximum Z and Y coordinates have been measured by the simulation model at the total temperature isoline of 2200 K to analyze the expansion rate of the shrouding combustion flame. The maximum axial and radial expansion rate of the shrouding combustion flame is defined as the ratio of maximum Z and Y coordinates of total temperature isoline of 2200 K, respectively, formed by the shrouding gas per second of the total heat value of the fuel shrouding jet. The maximum axial and radial expansion rate is addressed as the MAE-2200 and MRE-2200, respectively.

A higher MAE-2200 value indicates that there is a greater amount of high-temperature shrouding flame flowing alongside the main oxygen jet. This phenomenon suppresses the entrainment effect between the main oxygen jet and the ambient gas, while ensuring that the kinetic energy of the main oxygen jet remains unchanged.

The result shows that the MAE-2200 using H800, H720-N80, H720-C80, H560-N240 and H560-C240 was 9.06×10^{-5}, 8.77×10^{-5}, 8.23×10^{-5}, 7.82×10^{-5} and 6.09×10^{-5} m/MJ, respectively. When the shrouding mixed rate is 10% and 30%, the MAE-2200 generated by the H_2-N_2 shrouding mixed injection method is 1.07 and 1.28 times higher than that by the H_2-CO_2 shrouding mixed injection method. Thus, the decrease in MAE-2200 is attributed to a higher shrouding fuel mixed rate, resulting in reduced protective effectiveness of the shrouding combustion flame in the axial direction.

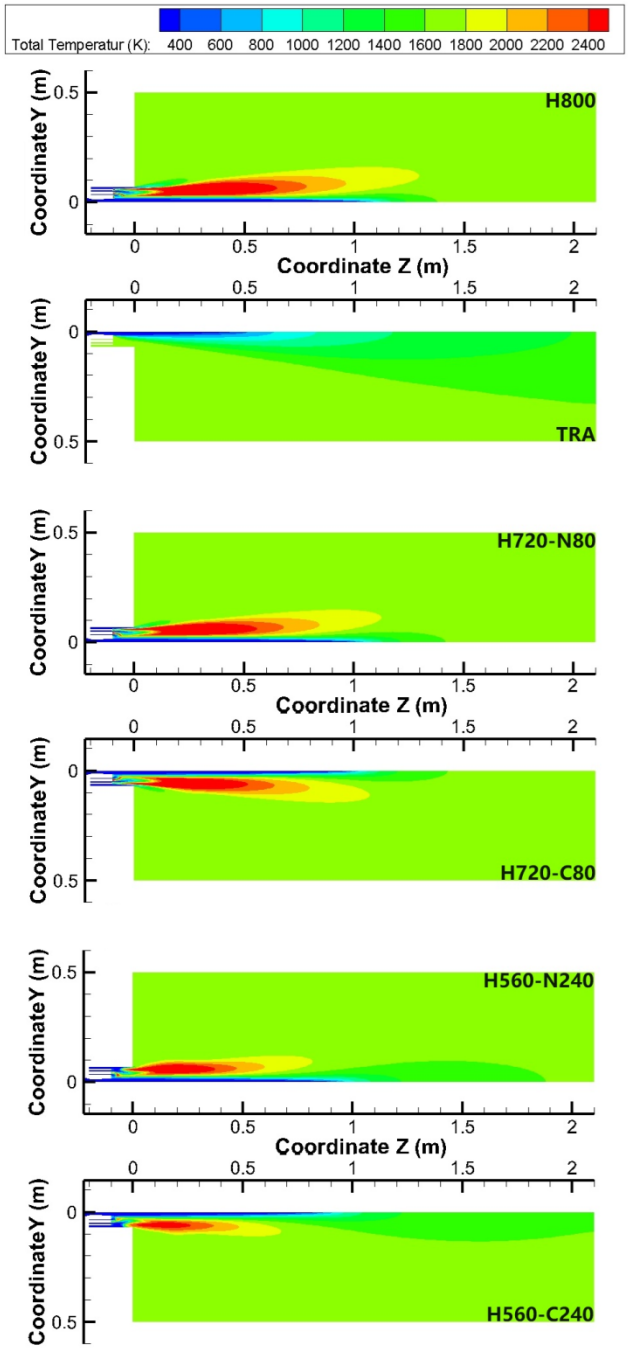


Figure 6. The total temperature of coherent jet profiles using different fuel mixed injection methods.

Compared with the H_2-CO_2 shrouding mixed injection method, the H_2-N_2 shrouding mixed injection method can increase the MAE-2200 of the coherent jet, which suppresses the entrainment effect between the main oxygen jet and the ambient gas. Thus, N_2 is a more suitable shrouding mixed gas type than CO_2.

A higher MRE-2200 represents that more thermal energy from the shrouding combustion flame has been transferred into the ambient gas, resulting in a reduction in the heat utilization of the shrouding fuel gas and in the impaction ability of the main oxygen jet.

Based on the simulation result, the MRE-2200 using H800, H720-N80, H720-C80, H560-N240 and H560-C240 was 1.17×10^{-5}, 1.22×10^{-5}, 1.19×10^{-5}, 1.43×10^{-5} and 1.37×10^{-5} m/MJ, respectively. Thus, the MRE-2200 is increased by a higher shrouding fuel mixed rate. This means that the ambient gas will absorb more thermal energy from the shrouding combustion flame, with a higher shrouding mixed rate.

When the shrouding mixed rate is 10% and 30%, the MRE-2200 generated by the H_2-N_2 shrouding mixed injection method is also 1.03 and 1.04 times higher than that by the H_2-CO_2 shrouding mixed injection method. Thus, compared with the H_2-N_2 shrouding mixed injection method, the H_2-CO_2 shrouding mixed injection method can suppress the radial heat transfer of the shrouding combustion flame.

Although the H_2-CO_2 shrouding mixed injection method reduces the radial heat transfer of the shrouding combustion flame, more thermal energy is consumed by the formation of the unstable intermediate reaction product, such as OH, CO and HCO, which reduces the protection effectiveness of the shrouding combustion flame for the main oxygen jet.

4.3. Impaction Cavity Parameters

The transfer of kinetic energy and oxygen mass between the molten bath and the coherent jet primarily occurs at the impaction cavity, due to the behavior of multiphase flow. This indicates that the shape of the impaction cavity significantly impacts the metallurgical technical indicators in the EAF steelmaking process.

There are two kinds of liquid flow, i.e., molten steel and liquid slag. Thus, the theoretical calculation model for these two-layer liquid phases has been adopted to calculate the impaction depth, with the following equations [26,27]:

$$H_p = \frac{P_d}{\rho_{slag} g},\ H_p < H_{slag}, \tag{4}$$

$$H_p = H_{slag} + H_{steel} = H_{slag} + \frac{P_d - \rho_{slag} g H_{slag}}{\rho_{steel} g},\ H_p \geq H_{slag}, \tag{5}$$

where H_p and H_{steel} are the theoretical impaction depth and steel molten penetrate depth (m), respectively. P_d is the dynamic pressure of the coherent jet (Pa). The gravitational acceleration (g) and liquid slag thickness (H_{slag}) are 9.81 m^2/s and 0.19 m, respectively. The liquid slag density (ρ_{slag}), and molten steel density (ρ_{steel}) are set as 3000 and 7000 kg/m^3, respectively.

Based on the coherent lance arrangement in a 120 t EAF structure, the lance height of the coherent is assumed to be 1.1 m, and its tilt angle is selected as 45°. This means that the distance between the coherent lance tip and the surface of the molten bath is about 1.56 m.

The maximum dynamic pressure of the coherent jet measured at a distance of 1.56 m from the coherent lance tip was derived from the simulation model. It is essential to acknowledge that this simulation model is the one constructed as detailed in Section 3, which is not a new simulation model, to calculate multiphase flow behavior. Subsequently, based on the maximum dynamic pressure of the coherent jet achieved in the simulation model, and the assumed data of molten steel and liquid slag, the theoretical impaction depth (H_p) can be calculated using Equation (5).

The theoretical impaction area is defined as the region, where the H_{steel} formed by the coherent jet is bigger than 0.005 m. Hence, the edge of the theoretical impaction area is achieved by a coherent jet dynamic pressure of 5935 Pa, according to the Equation (5). Consequently, the area in which the dynamic pressure of the coherent jet exceeds 5935 Pa has been determined from the simulation model, referred to as the theoretical impaction area. Figure 7 represents the theoretical impaction depth and area generated by different fuel mixed injection methods.

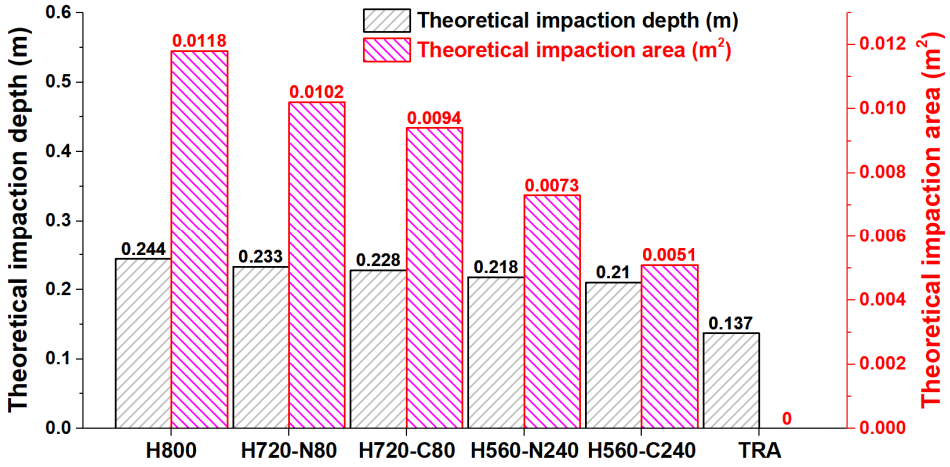


Figure 7. The theoretical impaction depth and area generated by different fuel mixed injection methods.

The result shows that both theoretical impaction depth and area are reduced with a higher shrouding mixed rate. For the H_2-N_2 and H_2-CO_2 shrouding mixed injection methods, the average reduction rate of the theoretical impaction depth and theoretical impaction area is 7.2% and 36.7%, respectively, when the shrouding mixed rate is increased from 10% to 30%. Thus, the shrouding mixed injection method has a greater influence on the theoretical impaction area than that on the theoretical impaction depth.

When the shrouding mixed rate is 10% and 30%, the theoretical impaction depth generated by the H_2-N_2 shrouding mixed injection method is 1.02 and 1.04 times deeper than those by the H_2-CO_2 shrouding mixed injection method, respectively. The theoretical impaction area formed by the H_2-N_2 shrouding mixed injection method with shrouding mixed rates of 10% and 30% are 1.09 and 1.43 times larger than those by the H_2-CO_2 shrouding mixed injection method, respectively. Hence, compared with the H_2-CO_2 shrouding mixed injection method, the H_2-N_2 shrouding mixed injection method can increase the theoretical impaction depth and area, at the same shrouding mixed rate. This trend is more obvious with a higher shrouding mixed rate.

Comparing the coherent jet, the traditional supersonic jet cannot penetrate the liquid slag layer, leading to a theoretical impaction area of 0 m^2, as shown in Figure 7. Based on the process of the oxygen mass transfer, the O element initially reacts with the Fe element in the liquid slag layer, resulting in the formation of (FeO). Subsequently, the (FeO) further undergoes displacement reactions with the elements [C], [P] and [Si] in the molten bath. Ultimately, the Fe element is reduced and enters the molten steel, and the [P] and [Si] elements are oxidized and transferred into the liquid slag. Simultaneously, the [C] element is oxidized into the CO or CO_2 gas, which then enters the furnace gas.

For the coherent jet, a portion of the oxygen gas can penetrate the liquid slag, reacting directly with the elements [C], [P], and [Si] in the molten steel. Therefore, as more oxygen gas penetrates the liquid slag, the utilization rate of oxygen elements is increased, leading to lower oxygen consumption and reduced smelting time in the EAF steelmaking process.

In this research, the effective flow rate of oxygen gas through the theoretical impaction area is calculated by the simulation model, which is addressed as the $F_{o\text{-}a}$, as shown in Figure 8. A larger $F_{o\text{-}a}$ indicates a higher oxygen utilization rate. The average $F_{o\text{-}a}$ generated by the 10% and 30% shrouding mixed rate is 80.2% and 62.5% of the $F_{o\text{-}a}$ generated by the H800, respectively. Thus, the $F_{o\text{-}a}$ is decreased with a higher shrouding mixed rate.

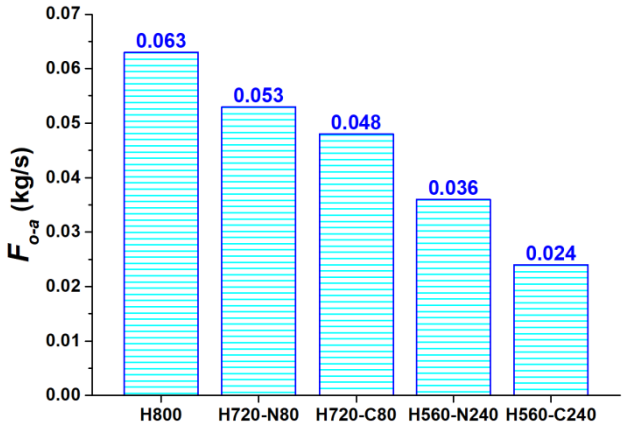


Figure 8. The effective oxygen flow rate through the theoretical impaction area using different fuel mixed injection methods.

Meanwhile, the $F_{o\text{-}a}$ generated by the H_2-N_2 shrouding mixed injection method is 1.1 and 1.5 times larger than that by the H_2-CO_2 shrouding mixed injection method, when the shrouding mixed rate is 10% and 30%, respectively. This indicates that the H_2-N_2 shrouding mixed injection method can improve the oxygen utilization rate, comparing with the H_2-CO_2 shrouding mixed injection method. Therefore, the oxygen flow rate is obviously reduced with a higher shrouding mixing rate. Comparing with the inert N_2, this trend is more evident when oxidizing CO_2 has been used.

5. Conclusions

This research focuses on enhancing the utilization efficiency of hydrogen (H_2), while minimizing its consumption. The conclusion of this research provides a fundamental understanding of coherent jets produced by the shrouding mixed injection method in high-temperature environments, specifically at 1700 K. The main conclusions of this research can be summarized as following:

1. Comparing with the traditional coherent jet, the total heat value of shrouding fuel gas is decreased using the shrouding mixed injection method. As a result, The axial velocity potential core length, $F_{o\text{-}a}$, theoretical impaction depth and area are all reduced with a higher shrouding mixed rate.
2. Oxidizing CO_2 will take part in the combustion reaction of the shrouding H_2, which reduces the combustion efficiency of shrouding H_2, leading to decreased the protective effect of the shrouding combustion flame in the axial direction. Thus, N_2 is a more suitable shrouding mixed gas type than CO_2.
3. The $F_{o\text{-}a}$, theoretical impaction depth and area generated by the H720-N80 is 84.0, 95.5 and 86.4% of those generated by the H800, respectively. Comparing with the H800, the H720-N80 may still lead to comparable production indexes in the EAF steelmaking process, which is still required to verify by the industrial application test.
4. While the primary conclusions are derived from laboratory investigations that have not been confirmed through industrial application testing, they nonetheless provide insights into the behavior of the coherent jet produced by various shrouding mixing methods. These findings may offer valuable guidance for the utilization of H_2 in the EAF steelmaking process.
5. In addition to achieving low-cost and large-scale production of green hydrogen, the storage and transportation of hydrogen energy within the steel enterprises present significant challenges. Consequently, addressing or mitigating hydrogen embrittlement is critical for the widespread adoption of hydrogen energy.

Author Contributions: Conceptualization, R.Z.; methodology, K.D.; software, F.L.; validation, none; formal analysis, G.W.; investigation, S.Y., F.L. and K.D.; resources, none; data curation, K.D.; writing—original draft preparation, S.Y. and F.L.; writing—review and editing, none; visualization, G.W.; supervision, R.Z.; project administration, R.Z.; funding acquisition, F.L. and G.W. All authors have read and agreed to the published version of the manuscript.

Funding: This research was funded by National Natural Science Foundation of China, grant number NSFC 52474343, NSFC 52322407, and NSFC 52293392.

Data Availability Statement: The original contributions presented in this study are included in the article. Further inquiries can be directed to the corresponding author.

Acknowledgments: The authors would like to express their thanks for the support by National Natural Science Foundation of China (NSFC 52474343, NSFC 52322407 and NSFC 52293392).

Conflicts of Interest: The authors declare no conflicts of interest.

References

1. Mitas, B.; Schenk, J. Oxygen distribution at the hot spot in BOF steelmaking. *Met. Mater. Trans. B* **2024**, *55*, 1680–1689. [CrossRef]
2. Yang, Z.; Yang, L.; Cheng, T.; Chen, F.; Zheng, F.; Wang, S.; Guo, Y. Fluid flow characteristic of EAF molten steel with different bottom-blowing gas flow rate distributions. *ISIJ Int.* **2020**, *60*, 1957–1967. [CrossRef]
3. Gokce, F.; Adar, C.; Tosun, M.A.; Isik, Z.; Gurbuz, A.E. Nitrogen control in scrap-based EAF steelmaking. In Proceedings of the AISTech 2024, Columbus, OH, USA, 6–9 May 2024; pp. 393–400.
4. Moreira, D.D.; de Souza, R.M.; Komati, K.S.; Sperandio, K.N.; Rodrigues, D.D.; de Oliveira, J.R. Study of the slag properties in steel dephosphorization in the EAF. In Proceedings of the AISTech 2024, Columbus, OH, USA, 6–9 May 2024.
5. Ramirez-Argaez, M.A.; Conejo, A.N. CFD study on the effect of the oxygen lance inclination angle on the decarburization kinetics of liquid steel in the EAF. *Metall. Res. Technol.* **2021**, *118*, 516. [CrossRef]
6. Alam, M.; Naser, J.; Brooks, G.; Fontana, A. Computational fluid dynamics modeling of supersonic coherent jets for electric arc furnace steelmaking process. *Met. Mater. Trans. B* **2010**, *41*, 1354–1367. [CrossRef]
7. Chen, Y.; Luo, Q.; Ryan, S.; Busa, N.; Silaen, A.K.; Zhou, C.Q. Effect of coherent jet burner on scrap melting in electric arc furnace. *Appl. Therm. Eng.* **2022**, *212*, 118596. [CrossRef]
8. Yamaguchi, M.; Yamamoto, Y.; Hagihara, Y. Functionalization of supersonic oxygen lance for EAF. In Proceedings of the AISTech 2021, Nashville, TN, USA, 29 June–1 July 2021; pp. 1592–1603.
9. Tian, B.; Wei, G.; Zhu, R.; Li, X.; Zhang, H. Energy balance and deoxidation status of electric arc furnace tapping processes. *Ironmak. Steelmak.* **2022**, *49*, 699–706. [CrossRef]
10. Wei, G.; Zhu, R.; Cheng, T.; Kai, D.; Yang, L.; Wu, X. Study on the impact characteristics of coherent supersonic jet and convention-al supersonic jet in EAF steelmaking process. *Met. Mater. Trans. B* **2018**, *49*, 361–374. [CrossRef]
11. Jung, J.; Gabriel, T.; Partyka, A.; Pavliš, M. Application of jet-burner technology for a small-sized EAF. In Proceedings of the AISTech 2021, Nashville, TN, USA, 29 June–1 July 2021; pp. 307–316.
12. Kourougianni, F.; Arsalis, A.; Olympios, A.V.; Yiasoumas, G.; Konstantinou, C.; Papanastasiou, P.; Georghiou, G.E. A comprehensive review of green hydrogen energy systems. *Renew. Energy* **2024**, *231*, 120911. [CrossRef]
13. Bian, J.; Zhou, Z.; Yu, J.; Shi, X.; Huang, P.; Du, W. A comprehensive energy flow analysis method based on hydrogen energy to electric energy conversion. *J. Phys. Conf. Ser.* **2024**, *2788*, 012004. [CrossRef]
14. Zaiter, I.; Ramadan, M.; Bouabid, A.; Mayyas, A.; El-Fadel, M.; Mezher, T. Enabling industrial decarbonization: Framework for hydrogen integration in the industrial energy systems. *Renew. Sustain. Energy Rev.* **2024**, *203*, 114782. [CrossRef]
15. Zhu, Y.; Keoleian, G.A.; Cooper, D.R. The role of hydrogen in decarbonizing U.S. industry: A review. *Renew. Sustain. Energy Rev.* **2025**, *214*, 115392. [CrossRef]
16. Feng, C.; Liu, F.; Zhu, R.; Kai, D.; Wei, G.; Tao, X. Computational investigation of coherent jet behavior generated by H_2 shrouding flow. *Metall. Mater. Trans. B* **2024**, *55*, 600–611. [CrossRef]
17. Mahoney, W.; Deneys, A.; Mathur, P.; Warty, S. The critical role of hydrogen in Linde's coherent jet technology. In Proceedings of the AISTech 2023, Detroit, MI, USA, 8–11 May 2023; pp. 566–576. [CrossRef]
18. Hu, S.; Zhu, R.; Dong, K.; Liu, R. Numerical simulation and industrial experimental research on the coherent jet with "CH_4 + N_2" mixed fuel gas. *Metall. Mater. Trans. B* **2018**, *49*, 2584–2598. [CrossRef]
19. Adam, A.M.; Bahamon, D.; Kobaisi, M.A.; Vega, L.F. Molecular dynamics simulations of the interfacial tension and the solubility of brine/H_2/CO_2 systems: Implications for underground hydrogen storage. *Int. J. Hydrogen Energy* **2024**, *78*, 1344–1354. [CrossRef]

20. Vadlamudi, S.; Gugulothu, S.K.; Panda, J.K.; Chalapathi, K.S.; Mohanty, D. An ideal investigation on conventional CRDI engine for optimum paradigm analysis of performance and exhaust emissions by using oxygenated and hydrogen fuel: An experimental green dual fuel approach. *Fuel* **2024**, *372*, 132160. [CrossRef]
21. Czylkowski, D.; Hrycak, B.; Miotk, R.; Dors, M.; Jasiński, M. Microwave plasma-assisted hydrogen production via conversion of CO_2-CH4 mixture. *Int. J. Hydrogen Energy* **2024**, *78*, 421–432. [CrossRef]
22. Sivells, J.C. Aerodynamic design of axisymmetric hypersonic wind-tunnel nozzles. *J. Spacecr. Rocket.* **1910**, *7*, 1292–1299. [CrossRef]
23. Smith, G.P.; Golden, D.M.; Frenklach, M.; Moriarty, N.W.; Eiteneer, B.; Goldenberg, M.; Bowman, C.T.; Hanson, R.K.; Song, S.; Gardiner, W.C.; et al. GRI-Mesh 3.0. Available online: http://www.me.berkeley.edu/gri_mech/ (accessed on 5 March 2025).
24. Mashruk, S.; Zhu, X.; Roberts, W.L.; Guiberti, T.F.; Valera-Medina, A. Chemiluminescent footprint of premixed ammonia-methane-air swirling flames. *Proc. Combust. Inst.* **2023**, *39*, 1415–1423. [CrossRef]
25. Liu, Y.; Gong, Y.; Guo, Q.; Tian, X.; Yu, G. Numerical study on OH* chemiluminescence in CH4/NH3 diffusion flame based on chemical kinetic mechanism. *Int. J. Hydrogen Energy* **2025**, *105*, 1230–1241. [CrossRef]
26. Qian, F.; Mutharasan, R.; Farouk, B. Studies of interface deformations in single- and multi-layered liquid baths due to an im-pinging gas jet. *Met. Mater. Trans. B* **1996**, *27*, 911–920. [CrossRef]
27. Li, M.; Li, Q.; Kuang, S.; Zou, Z. Determination of cavity dimensions induced by impingement of gas jets onto a liquid bath. *Met. Mater. Trans. B* **2016**, *47*, 116–126. [CrossRef]

Disclaimer/Publisher's Note: The statements, opinions and data contained in all publications are solely those of the individual author(s) and contributor(s) and not of MDPI and/or the editor(s). MDPI and/or the editor(s) disclaim responsibility for any injury to people or property resulting from any ideas, methods, instructions or products referred to in the content.